Journal Pre-proofs

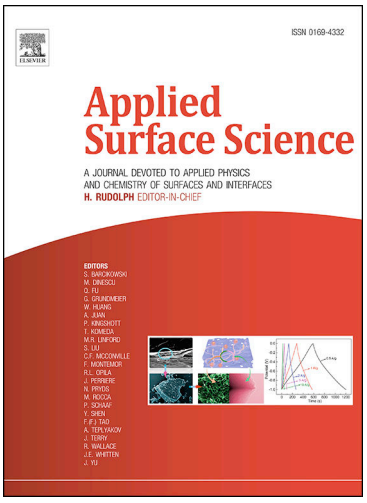

Full Length Article

Sensor Surface *via* Inspiration from Nature: The Specific Case of Electron Trapping in $TiO_2/WO_3(\bullet 0.33H_2O)$ and Reaction Center/$WO_3(\bullet 0.33H_2O)$ Systems

Bíborka Boga, István Székely, Monica Focşan, Monica Baia, Tibor Szabó, László Nagy, Zsolt Pap

PII: S0169-4332(21)02195-4
DOI: https://doi.org/10.1016/j.apsusc.2021.151139
Reference: APSUSC 151139

To appear in: *Applied Surface Science*

Received Date: 10 June 2021
Revised Date: 18 August 2021
Accepted Date: 29 August 2021

Please cite this article as: B. Boga, I. Székely, M. Focşan, M. Baia, T. Szabó, L. Nagy, Z. Pap, Sensor Surface *via* Inspiration from Nature: The Specific Case of Electron Trapping in $TiO_2/WO_3(\bullet 0.33H_2O)$ and Reaction Center/$WO_3(\bullet 0.33H_2O)$ Systems, *Applied Surface Science* (2021), doi: https://doi.org/10.1016/j.apsusc.2021.151139

Sensor Surface *via* Inspiration from Nature: The Specific Case of Electron Trapping in $TiO_2/WO_3(\cdot 0.33H_2O)$ and Reaction Center/$WO_3(\cdot 0.33H_2O)$ Systems

Bíborka Boga[a], István Székely[b,c,d], Monica Focșan[e], Monica Baia[b], Tibor Szabó[f,g], László Nagy[f] and Zsolt Pap[c, d, g *]

[a]Faculty of Chemistry and Chemical Engineering, Babeş-Bolyai University, Arany János 11, Cluj-Napoca, 400028, Romania

[b] Faculty of Physics, Babeş-Bolyai University, Mihail Kogălniceanu 1, Cluj-Napoca,400084, Romania

[c]Nanostructured Materials and Bio-Nano-Interfaces Center, Institute for Interdisciplinary Research on Bio-Nano-Sciences, Treboniu Laurian 42, Cluj-Napoca, 400271, Romania

[d]Institute for Research, Development and Innovation in Applied Natural Sciences, Babeş-Bolyai University, Fântânele 30, Cluj-Napoca, 400294, Romania

[e] Nanobiophotonics and Laser Microspectroscopy Center, Interdisciplinary Research Institute on Bio-Nano-Sciences, Babes-Bolyai University, Treboniu Laurean 42, Cluj-Napoca 400271, Romania

[f] University of Szeged, Department of Medical Physics and Biophysics, Rerrich Béla tér 1, Szeged, 6720, Hungary

[g]Isotope Climatology and Environmental Research Centre, Institute for Nuclear Research, Hungarian Academy of Sciences, Bem tér 18/c, Debrecen, 4026, Hungary

[h]Faculty of Science and Informatics, Department of Applied and Environmental Chemistry, University of Szeged, Rerrich Béla tér 1, HU-6720, Szeged, Hungary

*Corresponding author. Institute for Interdisciplinary Research on Bio-Nano-Sciences, Babeş-Bolyai University & Department of Applied and Environmental Chemistry, University of Szeged

E-mail address: zsolt.pap@ubbcluj.ro; pzsolt@chem.u-szeged.hu

Abstract

In this work, reaction centers (RCs) isolated from *Rhodobacter sphaeroides* purple bacteria was coupled with $WO_3(\cdot 0.33H_2O)$ *via* physical adsorption, where vectorial electron transfer (from RCs towards the inorganic carrier) was demonstrated using flash kinetics and photoluminescence measurements. The efficiency of the interaction between RCs and $WO_3(\cdot 0.33H_2O)$ was correlated to the components' surface charge at the working pH and the structural/morphological and surface properties of the inorganic carrier (e.g., anchoring capacity assured by H-O, W=O bonds). The role of $WO_3(\cdot 0.33H_2O)$ as final electron trap and charge separator was proven not only in RCs/$WO_3(\cdot 0.33H_2O)$ biohybrid systems but also in $TiO_2/WO_3(\cdot 0.33H_2O)$ composites. The charge transfer in the inorganic composites was evaluated by monitoring the reverse process of the color reaction ($W^{5+} \rightarrow W^{6+}$) *via* diffuse reflectance spectroscopy (DRS) after a previous UV-A (320-400 nm) exposure. The efficiency of the charge transfer process in inorganic systems was correlated to the initial W^{5+} content of $WO_3(\cdot 0.33H_2O)$, followed by the photocatalytic efficiency evaluation of these inorganic composites under UV-A irradiation.

Keywords: reaction center, hydrated tungsten trioxide, titania tungsten oxide composite, biohybrid, charge transfer, flash kinetics

Abbreviations

BChl – Bacteriochlorophyll; BPheo – bacteriopheophytine; CB – conduction band; CNT – carbon nanotubes; ΔE_g – band gap; FC – final complex; IEP – isoelectric point; ITO – indium tin oxide; k - apparent rate constant; LDAO – N, N-dimethyl-dodecyl amine-sulphate; MO – methyl orange; n- reaction order; OA – oxalic acid; P – dimer bacteriochlorophyll; P25 – commercial TiO_2; RC – photosynthetic reaction center; SP – supernatant, TRIS – 2-amino-2-hydroxymethyl-propane-1,3-diol; VB – valance band; X - conversion

1. Introduction

The integration of biological components exploiting unique peculiarities and properly engineered structures has led to creating specific structures such as bio-hybrid actuators and bio-hybrid sensors, contributing significantly to a sustainable development [1-2]. Among the great variety of biological systems, photosynthetic reaction center proteins (RCs) have received considerable attention from the scientific community due to their broad applicability in nano-bionics, optoelectronics, photonics, photovoltaics given by their high sensibility, selectivity, and high quantum yield [3]. RCs are transmembrane proteins with significant pigments and cofactors situated in the photosynthetic membrane of autotroph organisms (plants, some bacteria, and algae) [4]. Even if solar cell technology is a considerable application field of RCs because of their high quantum yield [3] (thus providing a solution for exhausting energy resources), their 'natural role' is related to the conversion of light into chemical energy, consequently contributing to food production [5].

Bacterial RCs are characterized with significantly lower structural complexity than the corresponding redox proteins from plants; thus, integrating bacterial RCs into different devices has remained a more attractive option. The unique peculiarities of bacterial RCs are assigned to the cofactors (bacteriochlorophyll – BChl; bacteriopheophytine – BPheo; ubiquinone 10 – Q_A, Q_B, non-heme type Fe^{2+}) within the protein. Light absorption induces vectorial electron transfer from the primary donor (P, dimer bacteriochlorophyll) to the secondary quinone (Q_B) through the formation of charge-separated species (e.g., P^+BPheo^-, $P^+Q_A^-$, $P^+Q_B^-$), followed by charge stabilization [6].

Even if these Nature's creations manifest unique properties, their stability issues can be considered a bottleneck in their application. To overcome this limitation, RCs were coupled with several inorganic carriers, namely TiO_2/WO_3 [7], ITO [8], Si [6], CNT [9], either by electrostatic adsorption or covalent binding [10], thus improving the stability of the whole biohybrid system. Among the coupling methods, adsorption is considered the simplest one [11]. However, its efficiency is doubtful since the protein structure could change its initial conformation [12]. Even if the possibility of conformation change exists, several cases were reported when the functionality of RCs remained unaffected [12] after bringing it in contact with Au [13], ITO [8]. Beyond conformation change, another vital issue in the case of adsorption is related to the surface charge

of components at the working pH, so the assessment of the isoelectric point (IEP) of components (e.g., , $IEP_{RC\text{-}R26}$ =6.1 [14]) is essential. .

WO_3 can be considered one of the most promising inorganic carriers for RCs due to its charge separation capacity and efficient electron acceptor in different composite systems. The conditions regarding the charge transfer from the RCs to $WO_3(\cdot 0.33H_2O)$ are also fulfilled: (i) its relatively high midpoint potential ensures the spontaneity of electron transfer from the redox protein to WO_3 [15-16], (ii) the energy of the generated holes on its valence band is relatively low, so there is no possibility for oxidizing the protein by the semiconductor [17]. Considering the aforementioned issues, the interaction between RCs and $WO_3(\cdot 0.33H_2O)$ was investigated within this work.

Mimicking the interaction of nature's creation (RCs) based biohybrid systems could be considered an efficient way to create certain sustainable systems. Several questions can be voiced within this topic: What would happen if an inorganic component would replace the previously described biological component of the biohybrid system? Which are the main criteria which should be fulfilled in order to have a similar operating principle? The answer lies mainly in the previously mentioned energetic criteria. Coupling of WO_3 with TiO_2 – in a well-determined ratio, using the corresponding method of preparation – either physical mixing [18] or pH adjustment corresponding to the surface charge of the components of the composite [19] is considered as an efficient way to prepare composites with great sensorial and photocatalytic efficiency (in certain cases, such as phenol, methyl-orange) [20-21]. According to Lee and coworkers, the excitation of TiO_2/WO_3 composites triggers the following steps [22]: (i) the excitation of semiconductors and the formation of charge carriers, (ii) charge-transfer (WO_3 *(h^+, e^-)* / TiO_2 *(h^+, e^-)* → WO_3 *(e^-)* / TiO_2 *(h^+)*), (iii) re-oxidation of W^{5+} to W^{6+} due to the involvement of molecular O_2. The degradation of pollutants could be realized either by indirect mechanism (involving reactive intermediates, such as ·OH, $\cdot O_2^-$) or direct hole oxidation [22].

The joint key component of the previously described biohybrid (RCs-based) and inorganic systems (TiO_2-based) is WO_3 because of its high affinity towards electrons (expressed by the terms of positive reduction potential) [23] and efficient charge separation capacity [18]. Tungsten trioxide has four well-known crystal phases: monoclinic, tetragonal, triclinic, and orthorhombic [20]. While the most common obtained crystal phase is monoclinic, the formation of thermodynamically unfavored crystal phases can be facilitated *via* shaping agents (e.g., NaCl [24],

K_2SO_4 [25]). The synthesis of partially hydrated crystals ($WO_3 \cdot nH_2O$, where n is either 0.33 or 0.50) with enhanced gas-sensing properties has also been reported, where the adjustment of hydration level is correlated to the precursor' concentration [26].

Although some RCs based biohybrid systems were investigated previously as described before), no relevant study focused on RCs/WO_3($\cdot 0.33H_2O$) composites; thus, this paper will offer a significant insight into this topic. Inspired by RCs/WO_3($\cdot 0.33H_2O$) biohybrid systems, the development of TiO_2/WO_3($\cdot 0.33H_2O$) inorganic systems with excellent sensorial properties will be presented within this paper.

2. Experimental

2.1. Materials

The synthesis of differently shaped WO_3 was carried out using: sodium chloride (NaCl, NORDCHIM, 99.5%), sodium tungstate dihydrate ($Na_2WO_4 \cdot 2H_2O$, Sigma Aldrich, 99%), HCl (hydrochloric acid, NORDCHIM, 37%, 12 M), ammonium metatungstate hydrate (AMT, $(NH_4)_6H_2W_{12}O_{40} \cdot xH_2O$, Sigma Aldrich, 99.99%).

Evonik Aeroxide P25 (Commercial TiO_2, Sigma Aldrich) was used to prepare TiO_2/WO_3 and TiO_2/$WO_3 \cdot 0.33H_2O$ composites. The photocatalytic efficiency of TiO_2/WO_3 ($\cdot 0.33H_2O$) composites was evaluated by the removal of oxalic acid (OA, HO_2C-$CO_2H \cdot 2H_2O$, Sigma Aldrich, 98 %) and of methyl-orange (MO, $C_{14}H_{14}N_3NaO_3S$, Sigma Aldrich) from aqueous solutions.

Chemicals used during isolation of the protein complex were N-dodecyl-N, N-dimethylamine oxide (LDAO, $C_{14}H_{31}NO$, Fluka), ammonium sulfate ($(NH_4)_2SO_4$, Sigma), diethylaminoethyl cellulose (DEAE-Sephacell, Sigma Aldrich).

The preparation of RC/WO_3($\cdot 0.33H_2O$) biocomposites (reagents for the dialysis and further washing steps) involved the following chemicals: 2-amino 2-hydroxymethyl propane-1,3-diol (TRIS, $NH_2C(CH_2OH)_3$, Aldrich), citric acid ($C_6H_8O_7$, VWR Chemicals), trisodium citrate dihydrate ($C_6H_5O_7Na_3 \cdot 2H_2O$, Chempur, analytical purity), Triton X-100 ($C_{14}H_{22}O$, Serva Feinbiochemica), polysucrose 400 (MP Biomedicals, LLC). The pH adjustment of buffer solutions (TRIS buffer at pH=8 and citrate buffer at pH=4) was realized either by the aqueous solution of NaOH (BioXtra, >98%) or HCl (hydrochloric acid, NORDCHIM, 37%, 12 M).

2.2. Synthesis of WO_3 (·0.33 H_2O) crystals

3.29 g $Na_2WO_4 \cdot 2H_2O$ and 1.16 g NaCl were dissolved in 75 mL distilled water to obtain partially hydrated crystals ($WO_3 \cdot 0.33H_2O$). The pH was adjusted to pH=2 by 3 M HCl under constant stirring and was followed by 24 hours of homogenization. Hydrothermal crystallization was carried out at 180 °C for 24 hours. It was followed by a washing step (centrifugal washing at 5000 rpm, 10 minutes), which facilitated the removal of undesired compounds. The obtained product was dried at 40 °C for 24 hours [20].

0.768 g $(NH_4)_6H_2W_{12}O_{40} \cdot xH_2O$ was dissolved in 12.5 mL 5 M HCl solution under continuous stirring for 15 min. The mixture was hydrothermally treated at 180 °C (4 h) and washed with water *via* centrifugation (3×10 min, 1600 rpm). The product was dried (80 °C, 12 hours) and thermally treated at 500 °C (30 min) in order to obtain an anhydrous crystal with a thermodynamically favored crystal phase (WO_3).

2.3. Preparation of TiO_2/WO_3(·0.33 H_2O) composites

The aqueous suspension of 760 mg TiO_2 (P25) and 240 mg WO_3 (WO_3, respectively $WO_3 \cdot 0.33H_2O$) (with a final volume of 50 mL) was stirred 4 hours at 500 rpm in order to achieve a stable pH and a homogeneous suspension, followed by drying at 80 °C, 12 hours [27].

2.4. Isolation of RC

The isolation of RC from *Rhodobacter sphaeroides R26* – as described previously by P. Maróti and C. A. Wraight [28] – was performed by a classical biochemical procedure that involves ultrasonic cell disruption, separation by (ultra)centrifugation, solubilization in LDAO, precipitation with ammonium sulfate, dialysis, fine purification by ion-exchange chromatography (DEAE Sephacell). The solubilized and purified protein complex has been stored at -20 °C.

2.5. The preparation of biocomposites

The mixture of an aqueous suspension of $WO_3(\cdot 0.33H_2O)$ (350 µL, 1 $g \cdot L^{-1}$) and RC (150 µL, 62 µM RC solubilized in LDAO) was dialyzed in the corresponding buffer solution (either in 10 mM TRIS 100 mM NaCl buffer for pH=8 or 20 mM citric acid/citrate buffer for pH=4) during constant stirring at 4 °C, 24 h. While removing ionic detergent (LDAO) was achieved through the semipermeable membrane during successive dialysis, the unbounded RCs were removed by

washing and centrifugation steps (adding 250 μL TRIS/citrate buffer with 0.03% Triton). Polysucrose 400 was added to the final complexes (at pH=4) to reduce the particles' sedimentation rate. The main steps of biocomposites' preparation are also presented in Fig. 3.a.

2.6. Apparatus

Scanning Electron Microscopy (**SEM**) was employed for the morphological and dimensional analysis of the studied sample. The measurements were carried out on a FEI Quanta 3D FEG microscope with 25 kV accelerating voltage.

The identification of the crystalline structure was accomplished by X-ray powder diffraction method (**XRD**) at a fixed wavelength (λ_{fixed}=1.5406 Å insured by Cu-Kα source) and in the range of the incident angle values between 10-50° (2θ°). The diffractometer (Rigaku Miniflex) was operated at 40 kV (tube voltage) and 30 mA (tube current) [29].

A Jasco-V650 spectrophotometer recorded the reflectance spectra (**DRS**) of the semiconductor oxides in the UV-Visible (250-1000 nm) region. The optical signal transformation into an electrical one was realized by an integration sphere (ILV-724). The device was applied in the determination of the band-gap values and monitorization of the W^{5+}/ W^{6+} species.

FT-IR and **Raman** spectroscopy were employed to determine the specific vibrational bands present in the structure of semiconductor oxides. The IR spectra of the studied samples (prepared previously in the form of pellets with KBr) were recorded at room temperature, in the range of 400-4000 cm^{-1}, by Jasco 6000 (Tokyo, Japan) spectrometer. Raman spectra of the samples were recorded with a multilaser confocal Renishaw inVia Reflex Raman spectrometer equipped with a RenCam CCD detector. The 532 nm laser was applied as an excitation source. The Raman spectra were collected using a 0.9 NA objective of 100× magnification. The integration time was 30 seconds, 1800 lines/mm grating for all spectra, and 10% of the maximum laser intensity – laser power of 20 mW. The spectral resolution was 4 cm^{-1}.

Flash-induced absorption change measurements were performed by a **locally designed single beam kinetics spectrophotometer** described previously by J. Tandori [30]. The absorption change could not be measured by continuous light due to the reversibility of charge recombination, so the studied sample was exposed to successive saturation flashes. The time interval between two successive flashes was set at 60 s. The specific measurement parameters were: I_0 = 100 mV, amplification: 100).

The **absorption spectra of RC** (in an equilibrium state and after excitation at $\lambda_{excitation}$ = 808 nm) in the range of 480-900 nm was recorded *via* a home-made Vis-NIR experimental setup equipped with a white light of DHL2000 light source as measuring light and CCD detector of a spectrophotometer (both from Avantes) and with a laser diode (2 W, 808 nm, Roithner). The details regarding this experimental setup were already described [31].

Fluorescence emission measurements were carried out by employing a Jasco FP-8600 High Sensitivity NIR spectrofluorometer with 1 nm spectral resolution and 10 nm excitation and emission bandwidths. The excitation source was assigned by a Xenon arc lamp as a light source, employing a fixed excitation wavelength at 850 nm, recording the spectra in the range of 860-1000 nm.

The photocatalytic reactions were carried out under UV-A irradiation (assured by 6 × 60 W fluorescence lamps with $\lambda_{maxemission}$ = 365 nm) for 2 hours, under continuous stirring. The photocatalytic efficiency of $TiO_2/WO_3(\cdot 0.33H_2O)$ composites ($c_{suspension}$ = 1 $g \cdot L^{-1}$) was tested in oxalic acid ($C_{0,\,OA}$ = 3 mM) and methyl orange ($C_{0,\,MO}$ = 125 μM) solutions. While the **Jasco V-650 spectrophotometer** has assured the qualitative analysis (at λ = 513 nm) of the MO degradation, the detection of OA was done by High-Performance Liquid Chromatography (**HPLC**) at λ = 206 nm. While the mobile phase was 0.06% aqueous solution of H_2SO_4 (with a flowrate of 0.8 $mL \cdot min^{-1}$), the stationary phase was a C16 column set up with Grom Resin ZH-type load. Merck-Hitachi D-7000 chromatograph and L-4250 UV-Vis detector are some important constitutive elements of HPLC.

3. Results and Discussion

3.1. Morphological/structural and optical characterization of WO_3 crystals used for the sensor

Analyzing the SEM micrographs, hierarchical structures of fiber-like (Fig. 1.a-b, $WO_3 \cdot 0.33H_2O$) and star-like (Fig. 1.c-d, WO_3) crystals were identified. While the diameter of hierarchical stars (WO_3) was 3.5-4.0 μm, the length of microfibers ($WO_3 \cdot 0.33H_2O$) varied between 2.5 and3.0 μm [20]. Taking a closer look, it can be observed that 10-15 nm thick nanowires were the building elements of the microfibers, which finally formed the microstar-like morphology. The morphology tailoring of $WO_3(\cdot 0.33H_2O)$ was assured by the combined effect of the precursor structure and working pH, which induced also the chemical transformation of the precursor ($W_{12}O_{41}^{10-} + 10H^+ \rightarrow 12WO_3 + 5H_2O$) [32]. It should be also mentioned that the synthesis procedure (temperature conditions, duration) also affected the morphology. However, some of the applied steps, such as the final thermal treatment (annealing), impacted the the ratio of the structurally intercalated water molecules. In contrast to the previous case, a 'capping agent' was added during the synthesis, which contributed to the preferential growth of the crystals alongside specific crystallographic directions, resulting finally nanofibers (showing 40-50 nm individual diameter) which self-assembled into bundles. The protons' contribution was also important as the following reactions shows: $WO_4^{2-} + 2H^+ \rightarrow H_2WO_4 \rightarrow WO_3 + H_2O$. To sum up, even if the building blocks of these hierarchical structures were nanofibers in both cases, it can be highlighted that the diameter of nanofibers was 3-4 times larger in the case of partially hydrated crystals than in the case of star-like particles [33].

Diffractograms of the WO_3 and $WO_3 \cdot 0.33H_2O$ samples were recorded between 10-50°angles to identify the crystal phase composition and calculate the primary mean crystallite size values (Fig. 1. e-f). Analyzing the reflections of $WO_3 \cdot 0.33H_2O$ sample – the characteristic 2θ positions were attributed to the following crystallographic planes: 13.88 (100), 22.74(111), 24.26 (110), 26.76 (101), 28.06 (200), 33.46 (111), 36.42 (210), 42.70 (300) and 49.66 (002) (JCPDS No. 33-1387).

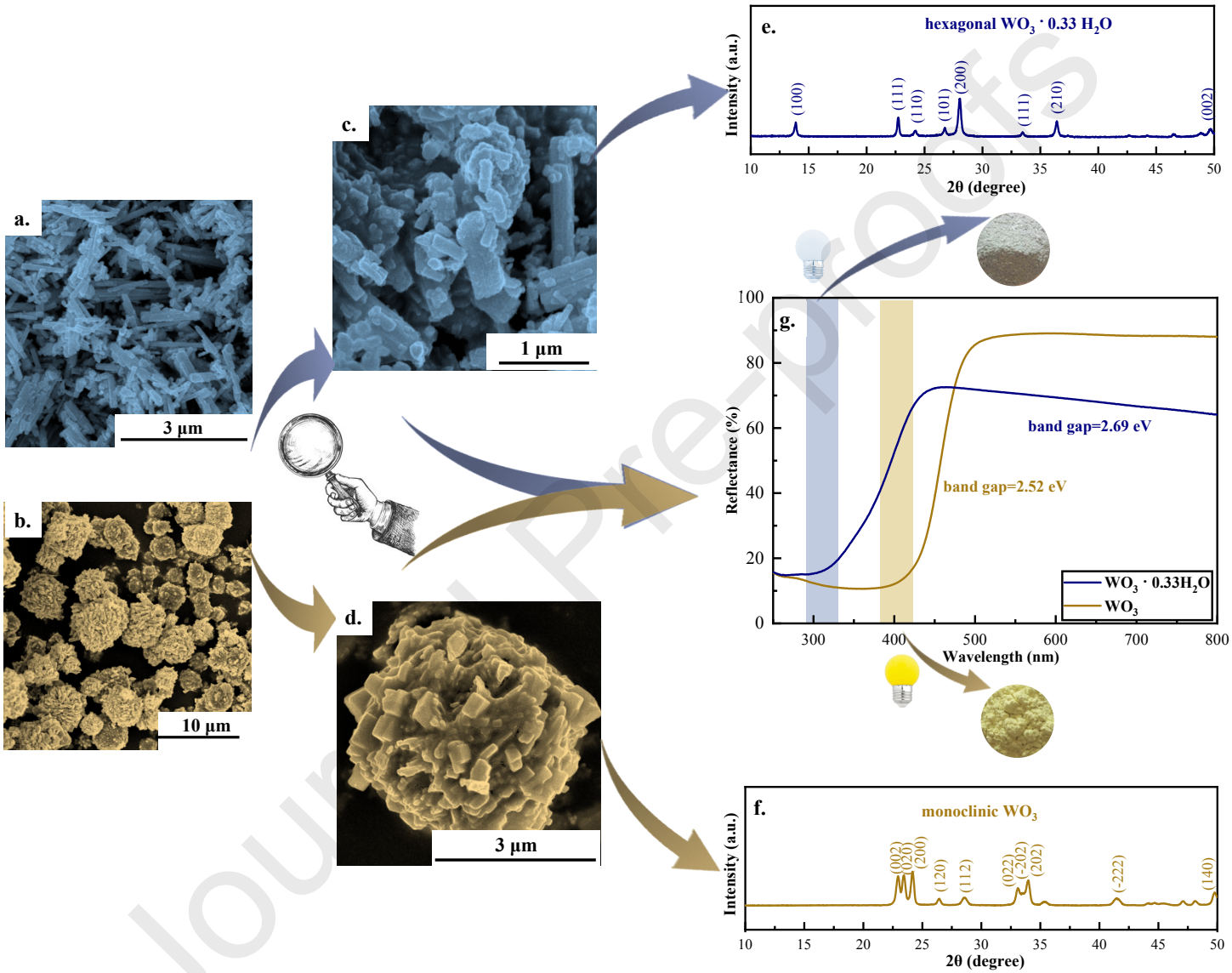

Fig. 1. (a-d) SEM micrographs, (e-f) XRD patterns, (g) DRS spectra of $WO_3 \cdot 0.33H_2O$ and WO_3

The primary crystallite size was ≈45 nm; however, a high aspect ratio difference (fiber-like structure) induces a significant error margin to the obtained value. The XRD pattern of $TiO_2/WO_3 \cdot 0.33H_2O$ composite was also recorded (Appendices, Fig. A1.) and the characteristic reflections of phases (hexagonal $WO_3 \cdot 0.33H_2O$, anatase and rutile TiO_2: JCPDS No. 84-1286 and No. 88-1175) were identified.

In the case of star-like crystals, the characteristic reflections (2θ°) were identified (JCPDS 97-001-6080) as follows: 22.94 (002), 23.46 (020), 24.16 (200), 26.44 (120), 28.52 (-112), 33.10 (222), 33.52 (-202), 33.98 (202), 41.48 (-222) and 49.76 (140). The characteristic dimension of the building blocks of microstars (diameter of fibers) determined from XRD was ≈20 nm with the same considerations. In a similar way, the coexistence of phases (monoclinic WO_3, anatase and rutile TiO_2: JCPDS No. 84-1286 and No. 88-1175) was proved in TiO_2/WO_3 system *via* XRD, presented in Fig. A1. (Appendices).

While the thermodynamically favored crystal phase – monoclinic – was identified in the case of star-like crystals [32], the arrangement of atoms into hexagonal crystal lattice [34] was facilitated by the shaping agent [20] in the case of fiber-like crystals. The Kubelka-Munk function was applied in order to determine the necessary energy for the translocation of an electron from the VB to CB (WO_3 2.52 eV→ λ = 550 nm, $WO_3 \cdot 0.33H_2O$: 2.69 eV → λ = 461 nm) (Fig. 1.g). The lower band gap value was observed in the case of the WO_3 sample [20].

3.2. Detailed structural analysis of WO_3

3.2.1. Raman spectroscopy

The characteristic bands were identified at 136, 244, 324, 682, 806, 941 cm^{-1} ($WO_3 \cdot 0.33H_2O$), respectively at 132, 256, 701 and 806 cm^{-1} (WO_3) in the recorded spectra (Fig. 2.a). While the vibrational band situated at 136 cm^{-1} ($WO_3 \cdot 0.33H_2O$) was assigned to lattice mode vibrations of the hexagonal partially hydrated crystal, the monoclinic lattice signal was evidenced at 132 cm^{-1} in the case of WO_3 crystals [35].

There were some well-defined differences between the two spectra. First of all, in the case of partially hydrated crystals, a relatively narrow band at 244 cm^{-1} corresponding to W-O-W bending vibrations of the bridging oxygen [36] and a low-intensity shoulder at 324 cm^{-1} could be identified as the specific band of $W\text{-}OH_2$ stretching vibrations mode [37]. In the case of WO_3, a

characteristic band identified in the neighborhood of the monoclinic lattice vibration (at 256 cm^{-1}) was assigned to O-W-O bending vibrations [27,38].

In the case of $WO_3 \cdot 0.33H_2O$, two relatively broad bands were identified at 682 cm^{-1} and 806 cm^{-1} that are characteristic signals for W-O-W and O-W-O stretching vibrations [39], the band situated at 682 cm^{-1} being also significant evidence for hexagonal semiconductor-oxide [40]. Two successive bands could be identified in star-like crystals: the highest intensity band (at 807 cm^{-1}) corresponded to the O-W-O stretching vibrations [37], while the characteristic signal at 701 cm^{-1} was assigned to W-O-W stretching modes. The characteristic band situated at 941 cm^{-1} was attributed to the symmetric stretching vibration of the terminal W=O bonds [41,42], which assures the anchoring capacity of $WO_3 \cdot 0.33H_2O$ crystals.

Considering that the band situated at 695-700 cm^{-1} was also assigned to specific stretching vibrations in W_2O_6, and W_3O_8 [35,43], the presence of W_2O_6 and W_3O_8 on the surface of the studied semiconductor-oxide could be demonstrated by analyzing this band. In order to highlight the differences given by the content of W_xO_y (x_1=2, y_1=6; x_2=3, y_2=8) on the surface of $WO_3(\cdot 0.33H_2O)$, the ratio between the intensities of the two successive bands (700, 800±20cm^{-1}) was evaluated. While the ratio (I_{682}/I_{806}) was 0.47 in the case of partially hydrated crystals, this ratio showed a lower value in monoclinic crystals: I_{701}/I_{806} =0.30. The significantly higher ratio in the sample $WO_3 \cdot 0.33H_2O$ highlights the presence of W_2O_6 and W_3O_8 on its surface [43].

3.2.2. IR spectroscopy

While active vibrations in Raman spectroscopy are related to the polarizability changes, the active vibrations are associated with the dipole moment in IR spectroscopy. Analyzing the FT-IR spectra of the semiconductor oxides (Fig. 2.b), the characteristic vibrational bands corresponding to the stretching vibration of O-W-O bonds ($WO_3 \cdot 0.33H_2O$ [44-45]: 755 and 826 cm^{-1}, WO_3 [27]: 823, 745 and 689 cm^{-1}) were identified. The relatively broad band assigned to the O-H stretching vibrations (3000-3500 cm^{-1}) [46], the H-O-H bending band (at 1600 cm^{-1}), and the O-H bending band (at 1634 cm^{-1}) were direct evidence for the presence of $WO_3 \cdot 0.33H_2O$. The anchoring capacity of $WO_3 \cdot 0.33H_2O$ was highlighted by the presence of a shoulder corresponding to W=O stretching modes (at 964 cm^{-1}) with a relatively weak intensity [47]. The band corresponding to W-OH_2 stretching mode (at 429 cm^{-1}) was also identified in the case of $WO_3 \cdot 0.33H_2O$ [37].

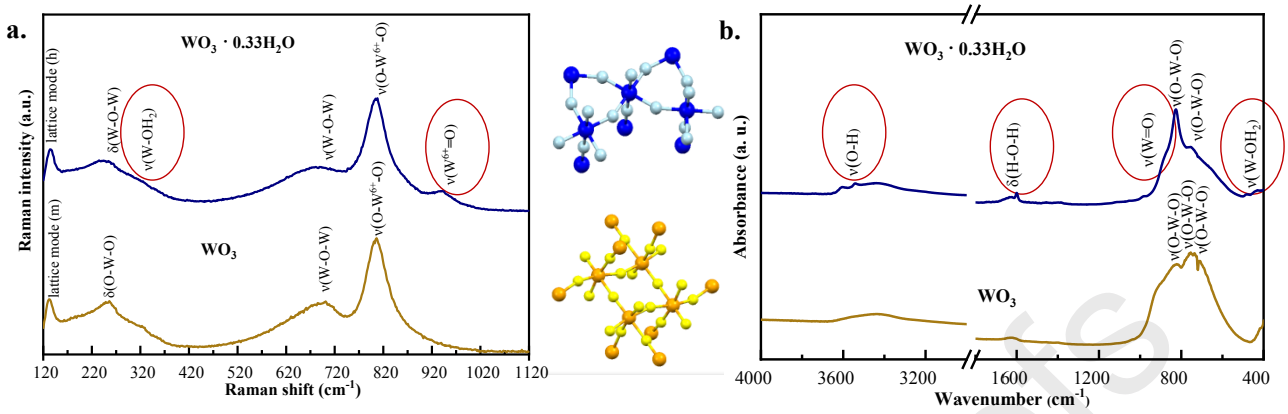

Fig. 2. (a) Raman and (b) IR spectra of partially hydrated and anhydrous WO_3

3.3. Inspiring from RCs coupled with WO_3 ($\cdot 0.33H_2O$)

The excitation of RC (in fact of the primary donor - P) can be realized through the absorption of photons whose energy is equal to the excitation energy of either cofactor in the visible range (BPheo: 525 and 760 nm; P and BChl: 600 nm, BChl: 800 nm, P:860 nm) because the characteristic absorption band of P is situated at 860 nm [48]. According to Fig. 3.b, the functionality of P was tested through its excitation *via* a monochromatic diode ($\lambda_{emission}$=808 nm). As a result of excitation, P^+ is formed, which induces the disappearance of the characteristic absorption band of P (λ=860 nm).

As mentioned in the introduction, coupling RC with different inorganic carriers is a promising way to enhance this redox protein's stability. $WO_3(\cdot 0.33H_2O)$ could be considered as an efficient inorganic carrier in RC/$WO_3(\cdot 0.33H_2O)$ biohybrid systems, due to:

(i) its relatively high midpoint potential, which ensures the spontaneity of electron transfer from the redox protein to WO_3 (E_m (WO_3) = 1.25 eV [49]) > E_m (Q_A,Q_B) = - 0.17 eV [50]),

(ii) the energy of the generated holes on its valence band is relatively low, so there is no possibility for oxidizing the protein complex by the holes of the semiconductor [17],

(iii) its absorption threshold is located near the visible range [20].

Hexagonal partially hydrated and monoclinic star-like WO_3 semiconductors were coupled with RC (as described previously in the 'Materials and methods' part and presented in Fig. 3.a) to investigate the as-obtained binary systems. While the partially hydrated WO_3 crystal was chosen due to its anchoring capacity (adsorption) assigned to the presence of W=O and O-H bonds on the surface of semiconductors (IR spectra, [51-52]), the star-like shaped WO_3 crystal was investigated

for the reason that it has contributed to the enhancement of photocatalytic efficiency of P25 in some cases [21].

3.3.1. Flash kinetics measurements

Relevant information about the redox state of the primary electron donor is obtained from flash-induced absorption kinetics measurements performed at its specific absorption band (860 nm) in the case of different fractions prepared at pH=4 and pH=8 [53]. Because of the pH dependence of free energy difference between $P^+Q_AQ_B^-$ and $P^+Q_A^-Q_B$states (ΔG_{AB}), the interpretation of the kinetic parameters (in terms of time constants and amplitudes) will be carried out separately at different pH values.

Furthermore, the amount of Q_B bounded to the RC can be influenced *by varying the surfactant concentration*, which is also highlighted by the value of the kinetic parameters [54]. Taking into consideration the fact that the solubility of quinone in a hydrophobic medium is favorable, it is evident that:

(1) when the concentration of the detergent has been increased, the kinetics describing the attachment/detachment it shifts to the direction of detachment; thus, the contribution of a slow component in the absorption decay after flash excitation is decreasing [55];

(2) without the corresponding concentration of LDAO, the quinone 'is stuck' on the binding site of Q_B, resulting in a high contribution and diminishing rate of recombination [55]. In addition, underneath the so-called critical micelle concentration (CMC_{LDAO}=1 mM≈0.02% [56]), the functionality of Q_B remains constant [55].

The time constant (τ_1) corresponding to the recombination of the primary component ($P^+Q_A^- \rightarrow PQ_A$) was fixed on 120 ms (=0.12 s) in both cases (at pH=4 and pH=8), which value allowed to evaluate the decay kinetics properly Because of the relatively significant differences in terms of concentrations, the supernatant fraction was diluted 10times at pH=8.

Case 1: The absorption kinetics measurements at pH=8

According to previous studies, considering the effect of relatively reduced surfactant concentration, the kinetics of charge recombination (measured at 860 nm) after a single Xe flash in the case of the reference sample at pH=8 (RC in Tris buffer solution) was described by two exponential terms representing the contribution and lifetime of fast (*circa* 9-10% and 120 ms) and

slow (*circa* 88% and 2-2.1 s) components [57].

The kinetics was analyzed *via* three exponential terms fit in the case of final complex fractions (FC), where the third component characterizing with a relatively large time constant (between 30-50 s) indicates the electron trap of a semiconductor oxide. The time constant values were not featured in Tables 1 and 2 because of their different magnitude compared to the time constants of fast and slow components. Not only the presence of the third exponential component (N_3 = 14.20% from N_{total}) but also the faster secondary time constant (τ_2=1.73 s) were significant evidence for the involvement of $WO_3 \cdot 0.33\ H_2O$ (Table 1, Fig. 3.c).

Besides, taking into consideration the fact that most of the LDAO was removed during the dialysis, but also the fact that only non-ionic detergent (Triton X-100) was added during the washing steps in preparation to remove the unbounded RC, it was expected to obtain high contribution and decreasing rate of recombination.

While the amount of RC attached on the surface of star-like WO_3 can be neglected at pH=8, there was a relatively reduced but detectable amount of RC (Van der Waals forces) adsorbed on the surface of partially hydrated semiconductor oxide. According to the previous morphological and structural analysis, this interaction can be attributed to the anchoring capacity of specific bonds (W=O, O-H) situated at the surface of $WO_3 \cdot 0.33\ H_2O$ [51].

Table 1. Fitting parameters of flash induced absorption change measurements at 860 nm (pH=8)

pH=8	REF(RC)	FC(RC+ $WO_3 \cdot 0.33\ H_2O$)	SP (RC+ $WO_3 \cdot 0.33\ H_2O$)
N_1(%)	15.46	15.46	17.57
τ_1 (s)	0.12	0.12	0.12
N_2 (%)	84.54	70.34	83.24
τ_2 (s)	2.50	1.71	1.93
N_3(%)	---	14.20	---

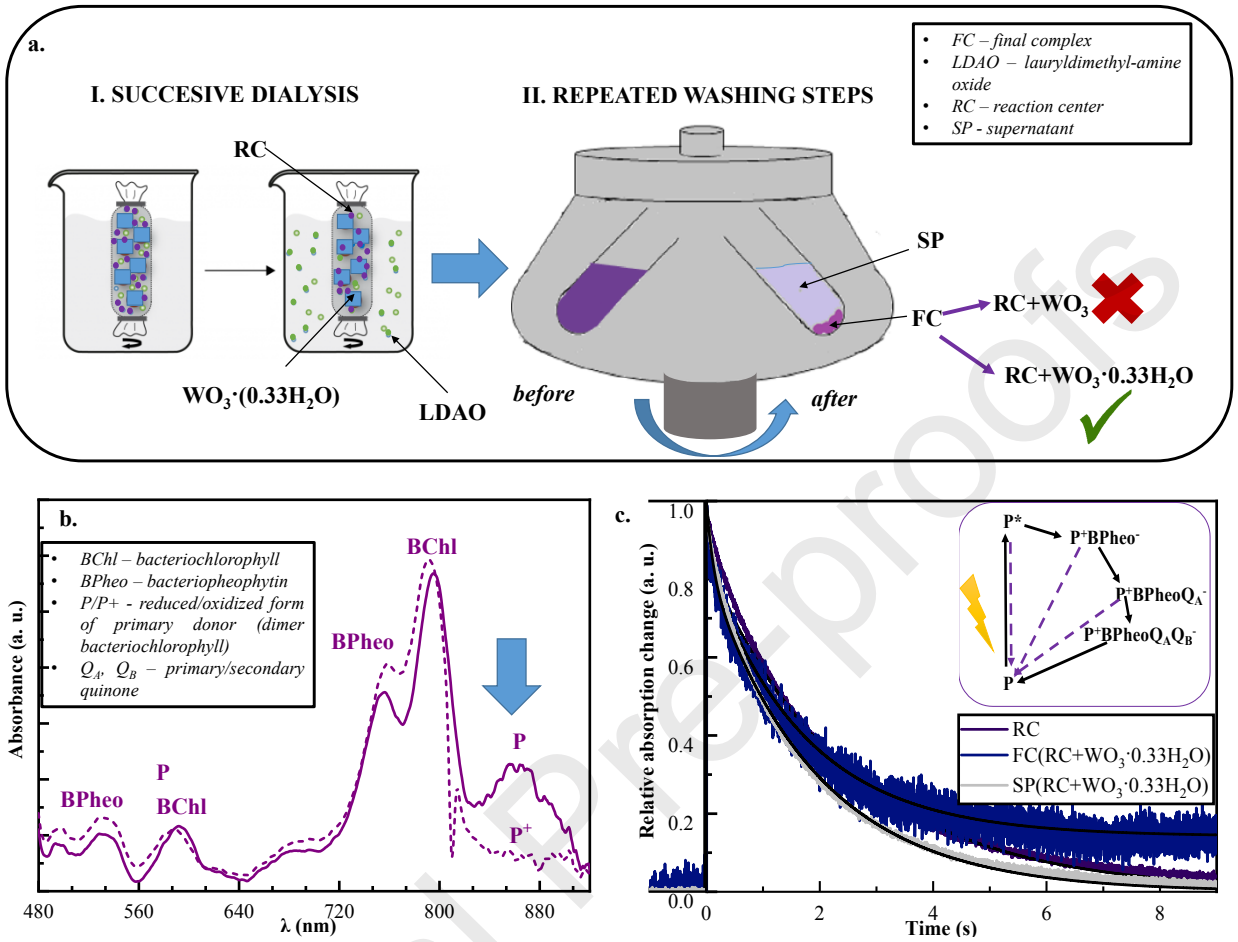

Fig. 3. (a) Preparation of biocomposites, (b) Absorption spectra before and after excitation at 803 nm, (c) Flash induced absorption change measurements at 860 nm (pH=8)

Case 2: The absorption kinetics measurements at pH=4

Although the free energy difference has a relatively large absolute value at pH=4 ($\Delta G_{AB} \approx$ -130 meV), its value is relatively low ($\Delta G_{AB} \approx$ -70 meV) and constant when the pH is situated between 6 and 9 [30]. According to this, the reference sample (RCs in citrate/citric acid buffer) at pH=4 was characterized *via* the corresponding kinetic parameters (Table 2).

A significant amount of RC was adsorbed on the inorganic carrier at pH = 4 (98% RC in RC/WO_3 and ~ 100% RC in $RC/WO_3 \cdot 0.33H_2O$) based on electrostatic interaction (given by different surface charges of the components, Fig. 4.a). The final complex fractions were diluted during the measurements; thus, the concentrations presented in Fig. 4.c-d are diluted concentration

values because of highlighting the differences in kinetic parameters in the case of different fractions (Table 2). Beyond the different surface charges of the components at his pH, pheophytization of a certain amount of P could also be observed in the structure of RC (Fig. 4.b).

Table 2: Fitting parameters of flash induced absorption change measurements at 860 nm (pH = 4)

pH=4	REF(RC)	FC(RC+$WO_3 \cdot 0.33\,H_2O$)	FC(RC+WO_3)	SP(RC+WO_3)
N_1(%)	5	3.21	4.2	---
τ_1 (s)	0.12	0.12	0.12	---
N_2(%)	91.6	66.40	65.80	100
τ_2 (s)	2.73	1.88	2.37	2.73
N_3(%)	3.5	40.80	30	---

To sum up, the relatively short time constant values (τ_2) describing the implication of secondary quinone ($P^+(Q_A^- Q_B \rightleftharpoons Q_A Q_B^-)$ and $P^+ Q_A^- Q_B \rightleftharpoons P^+ Q_A^- + Q_B$) were identified in the case of final complexes ($\tau_{2,\ FC,\ hydrated,\ pH=4} = 1.88$ s, $\tau_{2,\ FC,\ hydrated,\ pH=8} = 1.71$ s) (Table 2). Also, in both cases, the contribution of a third component indicated the role of $WO_3(\cdot 0.33H_2O)$ in the studied composites, namely the electron trap.

3.3.2. Emission fluorescence measurements

According to the previous luminescence studies of RCs, emission was observed at 918 nm given by the dimer bacteriochlorophyll (P), as a result of the excitation of RCs at $\lambda = 532$ nm [58]. Although the corresponding band of photoluminescence appeared in both cases (RC *vs.* biohybrid system) after excitation at $\lambda_{exc} = 850$ nm, there were some significant differences. First, while the response appeared at 918 nm in the case of RC (Fig. 4.e dotted spectrum), this value was shifted by 1 nm in the case of RC/$WO_3(\cdot 0.33H_2O)$ systems (Fig. 4.e brown spectrum). Besides, the significant broadening of the fluorescence emission band could be ample evidence for additional vibrational bands (implicitly the involvement of an additional component in the electron transfer) in the case of the RC/$WO_3(\cdot 0.33H_2O)$ system.

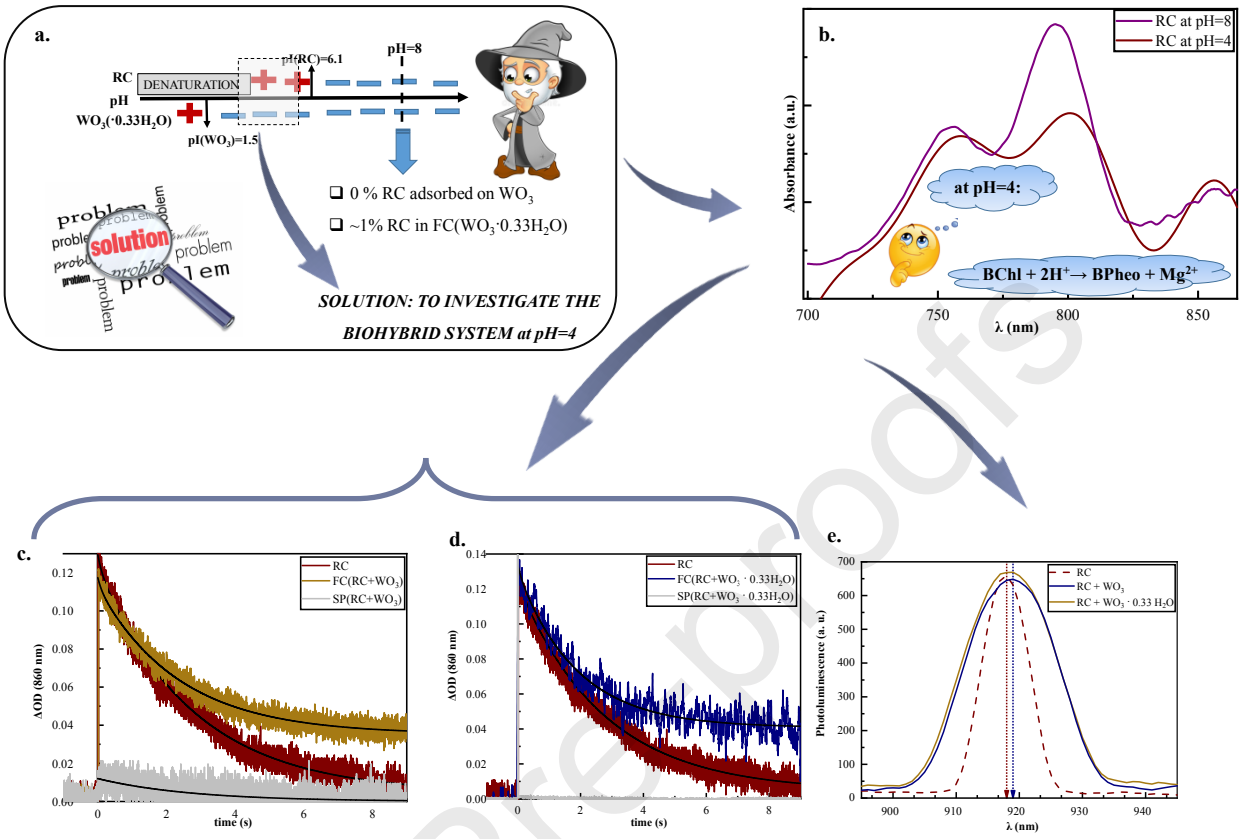

Fig. 4. (a) The surface charges of biohybrid system's components, (b) The absorption spectra of RC at different pH values, (c)-(d) Flash kinetics measurements of biohybrid system at 860 nm (pH=4), (e) Photoluminescence of different fraction

3.4. Charge transfer in $TiO_2/WO_3(\cdot 0.33H_2O)$ composites

The latter mentioned properties of $WO_3(\cdot 0.33H_2O)$, namely affinity towards electron, stabilization of the separated charges, assures the applicability of $TiO_2/WO_3(\cdot 0.33H_2O)$ composites not only as an efficient photocatalyst, but also as a qualitative sensor for some pollutants, either in the liquid phase (e. g. oxalic acid), or in the gaseous phase. As described before, the reduction of W^{6+} was induced by a quantum of energy, determined by the electron transfer from TiO_2 to $WO_3(\cdot 0.33H_2O)$. This charge transfer is reversible in the presence of species with high affinity to electrons (e.g., molecular oxygen).

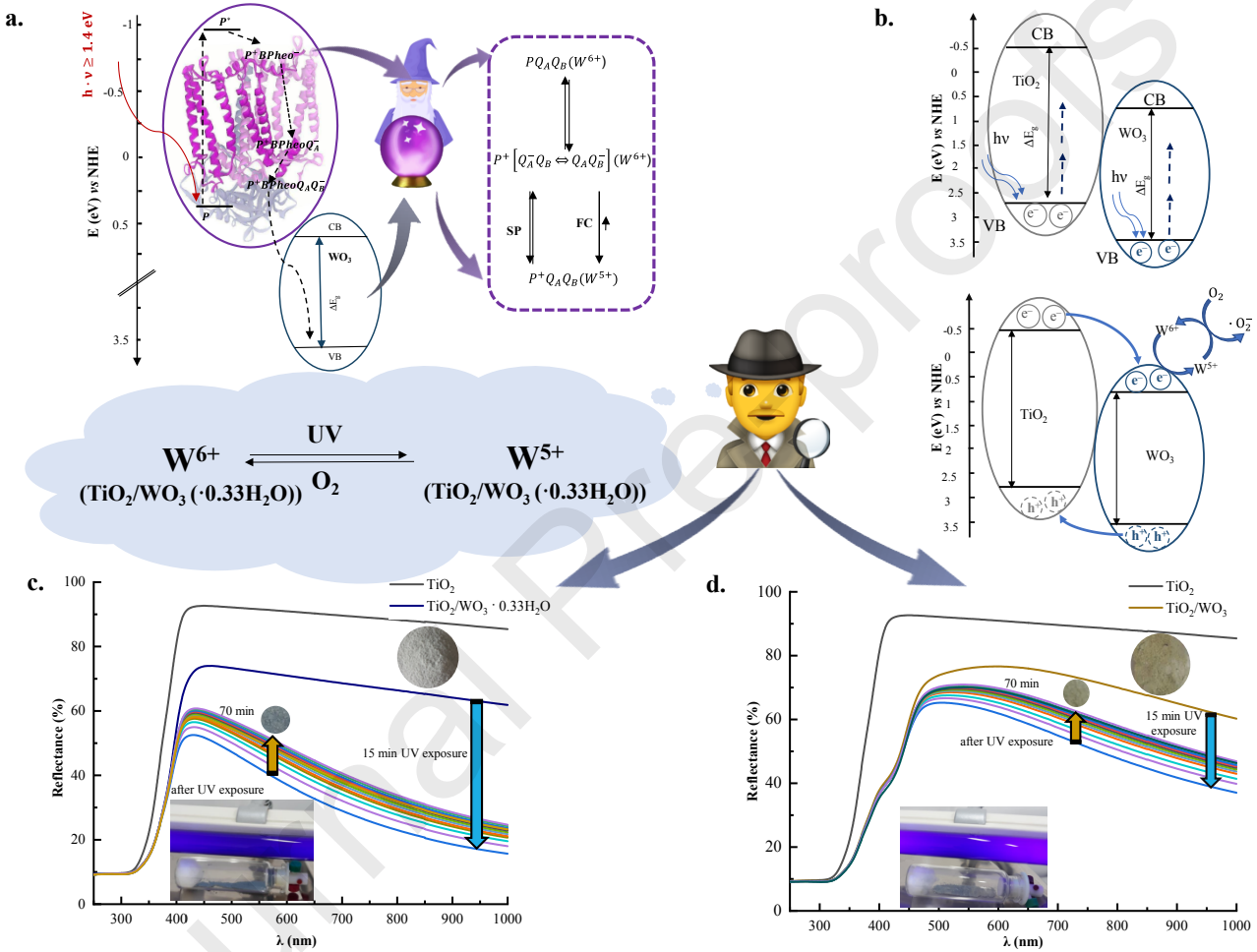

Fig. 5. (a) The schematic representation of charge transfer in RC/WO_3(·0.33H_2O), (b) The schematic representation of charge transfer in TiO_2/WO_3(·0.33H_2O) composites, (c)-(d) The reflectance spectra of TiO_2/WO_3·0.33H_2O and TiO_2/WO_3 before and after UV irradiation

The next question would be: how can we monitor spectroscopically the charge transfer in the latter mentioned inorganic systems (in other words the formation of W^{5+} centers) in the most convenient way? In this work, we propose the recording of the reflectance spectra (DRS) in the UV-Vis-NIR range at certain well-defined moments, because while the absorption maximum of W^{6+} centers is situated at 340 nm, this value is 970 nm in the case of W^{5+} centers [59].

First, the DRS spectra of the composites before UV irradiation were recorded (Fig. 5.c - dark blue spectra– $TiO_2/WO_3 \cdot 0.33H_2O$, Fig. 5.d – golden spectra – TiO_2/WO_3). Although the reflectance remained constant in the 550-900 nm domain in the case of $TiO_2/WO_3 \cdot 0.33H_2O$ composite without any excitation, a significant decrease of reflectance in the same domain was observed after 15 min UV-A exposure (Fig. 5.c). The charge transfer from TiO_2 to $WO_3(\cdot 0.33H_2O)$ (implicitly the reduction of W^{6+} to W^{5+}) was induced by the presence of ethanol vapors and UV-A irradiation (315 - 400 nm) during 15 min, in a specific isolated vial, followed by the immediate recording of the DRS spectra (Fig. 5.c-d) The quantification reduction or colorization process ($W^{6+} \rightarrow W^{5+}$) of TiO_2/WO_3 ($\cdot 0.33H_2O$) composites was carried out *via* the computation of the relative reflectance difference ($(R_0-R_{UV})/R_0$) at 970 nm considering the initial reflectance value (R_0) and also after UV irradiation (R_{UV}). While the relative reflectance difference corresponding for the direct process ($W^{6+} \rightarrow W^{5+}$) was 73.72% in the first case ($TiO_2/WO_3 \cdot 0.33H_2O$), this value was significantly lower (37.90%) in the second case (TiO_2/WO_3), which is clear evidence for the enhanced formation of W^{5+} centers in the first case as it can be seen in Fig. 5.c.

The reverse process ($W^{5+} \rightarrow W^{6+}$) was also monitored *via* DRS in well-defined moments (2-14 in 2/4 minutes, 14-39 in 5 minutes, 39-59 in 10 minutes). The quantification of reverse process was interpreted *via* $(R_0-R_{70})/R_0$ considering the reflectance value after 70 min after UV irradiation (R_{70}) and the initial reflectance value (R_0). Because of the fact that the later mentioned relative reflectance difference was approximately three times higher in the case of $TiO_2/WO_3 \cdot 0.33H_2O$ composites (61.30%) in comparison to TiO_2/WO_3 (22.60%), resulting that the reverse process was not completed even after 70 min in the first case (Fig. 5.c), while the decolorization was almost completed in the second case (Fig 5.d). The closer completion of $W^{5+} \rightarrow W^{6+}$ process in TiO_2/WO_3 systems after 70 min can be explained by the weaker homogeneity of W^{5+} centers after 15 min UV-A exposure.

The differences in reduction and re-oxidation ($W^{6+} \xrightarrow{h\nu} W^{5+}$, $W^{5+} \rightarrow W^{6+}$) were given by the following issues: (i) the ratio of W^{5+}/W^{6+} is higher in the case of $WO_3.0.33H_2O$ than in the case

of WO_3 [60] in the fundamental state, without any excitation, (ii) structural and morphological differences of WO_3 crystals.

3.4.1. Testing the functionality of the TiO_2/WO_3 composites *via* photocatalysis

The electron transfer process from TiO_2 towards the different tungsten oxide – based components is one of the crucial steps in the degradation of model pollutants with these composites. The photocatalytic efficiency of TiO_2/WO_3 ($\cdot 0.33H_2O$) composites for the removal of oxalic acid (OA) and methyl orange (MO) from aqueous solutions was tested and analysed [18]. The proposed mechanism of photocatalytic processes in TiO_2/WO_3 composites [18,61]:

1. Generation of holes/electrons:

$TiO_2 + h\nu \rightarrow TiO_2 + (h^+ + e^-)$, $WO_3 + h\nu \rightarrow WO_3 + (h^+ + e^-)$

The generation of charge carriers involves two steps: (i) the photoexcitation of valence band electrons (e_{vb}^-) of the photocatalyst ($h \cdot \nu \geq \Delta E_g$, where $\Delta E_{g,TiO_2} = 3.2$ eV, $\Delta E_{g,WO_3 \cdot 0.33H_2O} = 2.69$ eV, $\Delta E_{g,WO_3} = 2.52$ eV), (ii) translocation of (e_{vb}^-) into the conduction band, thus generating holes on the valence band (h_{vb}^+) and electrons on the conduction band (e_{cb}^-) (Fig. 5.b). In Fig. 5.b, the positions of the band edges are depicted corresponding to $WO_3 \cdot 0.33H_2O$ [60].

2. Charge transfer:

WO_3 *(h^+, e^-)* / TiO_2 *(h^+, e^-)* → WO_3 *(e^-)* / TiO_2 *(h^+)*

While the photogenerated electrons from the CB of TiO_2 are transferred to the WO_3 conduction band, the photogenerated holes are translocated from the WO_3 VB to the TiO_2 VB. In other words, the VB of both oxides are at the disposal for the holes, and the CB of WO_3 acts as an electron trap [61,62]. In the absence of WO_3, the photogenerated e^- would be transferred to the Ti^{4+} sites ($Ti^{4+} + e^- \rightarrow Ti^{3+}$), and the recombination of h^+ with O^{2-} sites would occur ($2O^{2-} + h^+ \rightarrow O_2$), which would lead to the release of molecular oxygen from the surface [63]. On the other hand, if only $WO_3(\cdot 0.33H_2O)$ would be present, then similar processes would occur – namely the formation of molecular oxygen, however recombination would not be observed because photogenerated electrons would remain alone [63-64].

3. *Reduction of W^{6+} into W^{5+} followed by the reoxidation of W^{6+}*

$W^{6+} + e^- \rightarrow W^{5+} W^{5+} \rightarrow e^-(O_2) + W^{6+}$

Simultaneous degradation and detection of OA was achieved during the photocatalytic process due to the formation of W^{5+} species, which was visible by the bluish colour for the suspension.

Due to the advantageous redox potential of OA and the valence band redox level (*vs* standard electrode) of investigated semiconductors (TiO_2, $WO_3(\cdot 0.33H_2O)$), direct hole oxidation is also a possible pathway for OA degradation *via* $TiO_2/WO_3(\cdot 0.33H_2O)$. Considering the pK_a values of OA (pK_{a1}=1.27 and pK_{a2}=4.28), the deprotonation of OA (thus resulting oxalate) is obvious in an aqueous solution [65].

Direct hole oxidation involved the oxidation of oxalate to oxalate radical, followed by the formation of formate radicals *via* decarboxylation as it was presented in Fig. 7.a [66]. The next step is either the formation of formic acid (which can be decomposed into CO_2 and H_2O) or directly CO_2 [66]. Considering the role of OA in the presented mechanism, it can be considered as 'sacrificial electron donor' or 'hole scavenger' [67]. The indirect mechanism through radicals is also a possible scenario for its degradation, which involves the formation of the same intermediates as in the first case.

The degradation of MO most probably is accomplished through an indirect mechanism involving free radicals [68]. The mechanism includes the breaking of the azo bond and the involvement of the reactive oxygen species (radicals)in the generation of hydroxylated species (e.g., dihydroxylated form of 4-aminobenzenesulfonate, monohydroxylated form of 4-diazenylbenzenesulfonate, tetrahydroxylated form of aniline, hydroquinone) [69,70]. The final products after photodegradation are CO_2 and H_2O [69-70]. The possible detailed mechanisms of MO degradation are presented in Fig. A2 (Appendices).

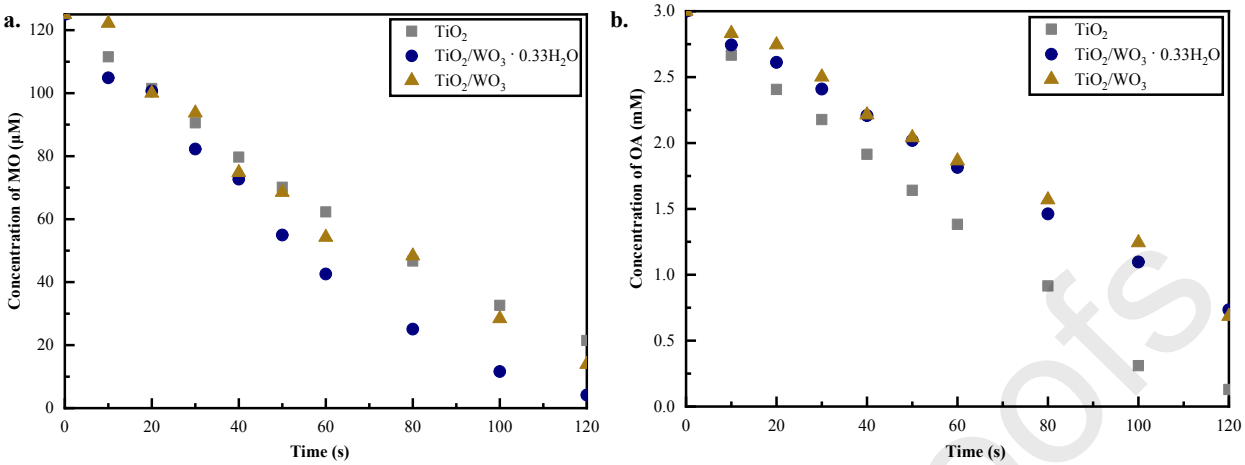

Fig. 6. (a) Degradation curves of MO (b) Degradation curves of OA under UV irradiation

The photocatalytic efficiency of the composites (in both cases ≈77 %) after 2 hours was lower than that of the reference (commercial TiO_2, X ≈ 96%) in the case of OA degradation (Table 3, Fig. 6.b). In contrast, $TiO_2/WO_3 \cdot 0.33H_2O$ composite has been considered the most efficient catalyst for MO degradation with a conversion of ≈97%, after 2 hours, under UV exposure and continuous stirring (Fig. 6.a). The highest reaction rate is attributed to $TiO_2/WO_3 \cdot 0.33H_2O$ during MO degradation (Table 3). Even if a higher reaction rate could be observed in composite systems during OA degradation, the conversion rate in these cases was lower. The higher photocatalytic efficiency of $WO_3 \cdot 0.33H_2O$ could be explained by the presence of W_xO_y on its surface, which ensures enhanced mobility for electrons, but also by the higher percentage of W^{5+} ($WO_3 \cdot 0.33H_2O$: 4.05%, WO_3: 2.35%).

Table 3: Kinetic and photocatalytic properties of composites and reference catalyst during MO and OA degradation

Sample	n	R^2	$k \cdot 10^2$, $OA:\left(\frac{mM}{min}\right)^{1-n}$; $MO:\left(\frac{\mu M}{min}\right)^{1-n}$	X(%)
$TiO_2/WO_3 \cdot 0.33H_2O$ (OA)	0	0.9926	1.89	77.21%
TiO_2/ WO_3 (OA)	0	0.9926	1.89	77.21%
TiO_2 (OA)	0.25	0.9947	1.76	95.68%

TiO_2/ WO_3·0.33H_2O (MO)	0.5	0.996	7.79	96.69%
TiO_2/ WO_3 (MO)	0.5	0.9874	6.15	88.88%
TiO_2 (MO)	0.5	0.9997	5.43	82.80%

3.5. The practical applicability of TiO_2/WO_3 systems – Mimicking the nature

Considering the previous experiments related to the identification of ethanol vapors in a closed system using TiO_2/WO_3 composites, the next question did arise: is it possible to apply TiO_2/WO_3 composites as sensors in open systems as well? In order to answer this question, the following simple experiment was carried out, in which on a 5 (cm) × 5 (cm) plain household tin foil 2 mL WO_3 and, 2 mL TiO_2 aqueous suspension ($C = 10\ g \cdot L^{-1}$) was deposited on different sides of the tin foil followed by drying for 5 hours at room temperature. This procedure was repeated twice.

Furthermore, 1 mL of 5 mM oxalic acid solution was dropped onto the titania-coated side. The coated tin foil was placed under sunlight, and immediately, the foil side which contained WO_3 turned blue (Fig. 7.b). To explain this phenomenon a charge transfer mechanism was conceived and detailed as follows. Charge carriers were generated in the VB (h^+) and CB (e^-) of the semiconductors due to solar light irradiation. The photogenerated holes from the VB of the TiO_2 oxidized OA into oxalate radical at the moment when the solvated OA reached the TiO_2 particles (Fig. 7.a, c). The oxidation product was also an electron, which was transferred from TiO_2 to a W^{6+} center through the tin foil (conductor), thus reducing W^{6+} into W^{5+}. The blueish coloration of the WO_3 coated tin foil was due to the formation of W^{5+} centers, as it was demonstrated previously *via* DRS measurements.

Thus, the question related to the applicability of the inorganic systems was answered, namely TiO_2/WO_3 systems can be used as qualitative sensors not only in the case of perfectly closed systems but also in the case of open systems. Moreover, this experiment demonstrated that TiO_2/WO_3 systems can be used as qualitative sensors not only for ethanol but also for oxalic acid. The identical coloration was observed in oxalic acid suspension (with TiO_2/WO_3 catalyst) under UV irradiation (Supplementary Information – video).

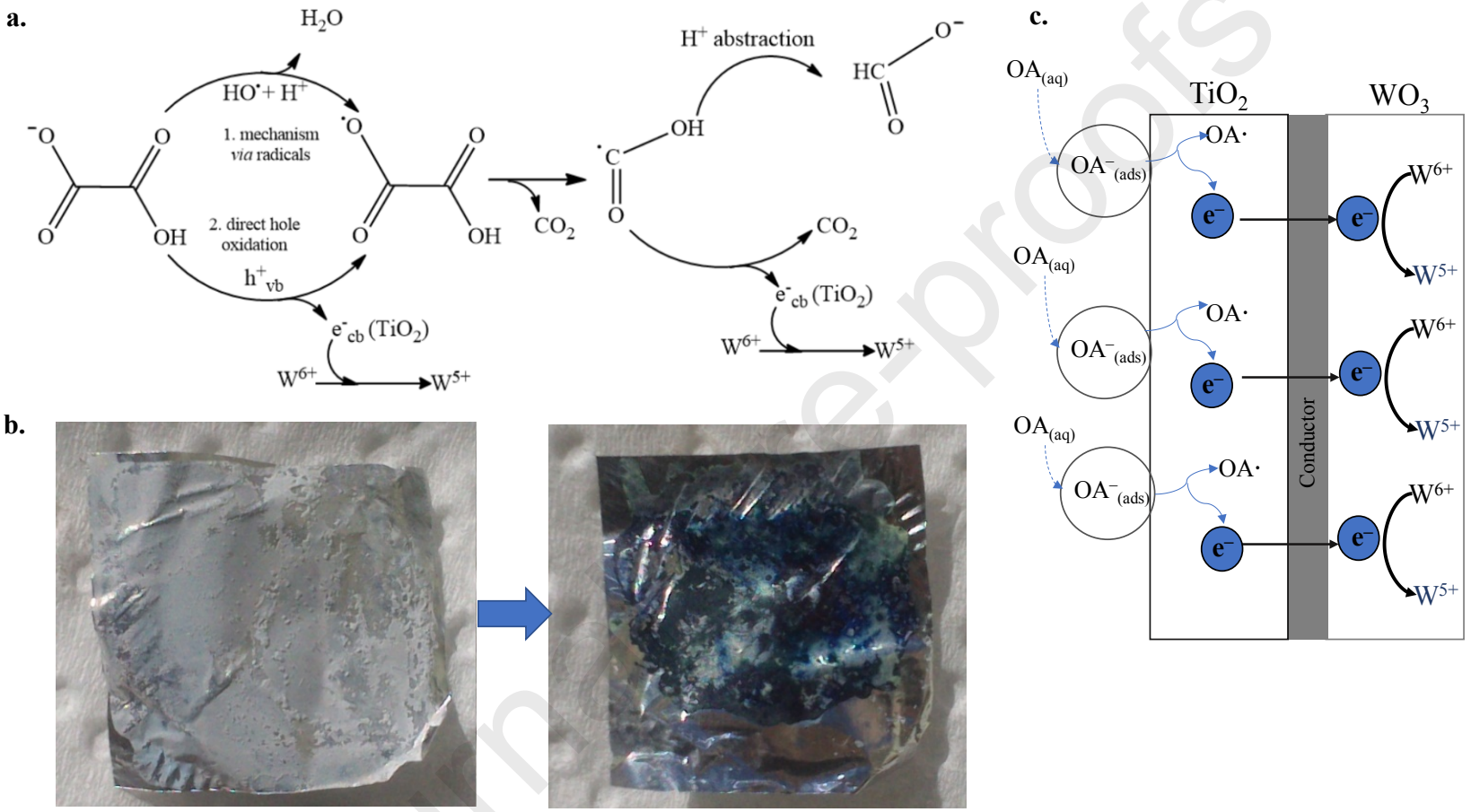

Fig. 7. (a) The mechanism of OA photodegradation and detection, (b) The coloration of WO_3 side (of tin foil) before and after oxalic acid addition, (c) The schematic representation of the mechanism

3. Conclusions

This work can be considered as a comparative study of specific photoinducible WO_3-based composites (biohybrid RC/WO_3($\cdot 0.33H_2O$) and inorganic TiO_2/WO_3($\cdot 0.33H_2O$) systems), where the functionality of the final (common) electron trap were analyzed and discussed from different point of views. This study offers valuable insight into the effect of different structural, morphological, optical peculiarities of anhydrous and partially hydrated WO_3 crystals on the interaction between the latter mentioned carrier and RCs, respectively TiO_2.

It was proved that morpho-structural peculiarities of WO_3($\cdot 0.33H_2O$) (in particular the presence of W=O, O-H bonds on the surface of semiconductor) and the surface charge of the components had significant influence on the interaction between RC and WO_3 ($\cdot 0.33H_2O$). The involvement of WO_3($\cdot 0.33H_2O$) in the photoinduced electron transfer in the biohybrid system was highlighted *via* the broadening of the characteristic fluorescence emission band (at 920 nm) but also *via* the analysis of the fitted kinetic parameters (shorter secondary time constants).

A particular experimental procedure was developed to quantify the electron trap's efficiency in inorganic systems, where the semiconductor's trapping ability was correlated to its ground state W^{5+} content. The importance of this charge transfer in TiO_2/WO_3($\cdot 0.33H_2O$) systems relies on simultaneous detection and efficient degradation of certain pollutants.

Acknowledgment

The authors express special thanks to Zsejke-Réka Tóth (Ph.D. Student), Enikő Bárdos (Ph.D. Student), Tamás Gyulavári (Ph.D. Student) for the SEM micrographs, Kata Saszet (Ph.D. Student), Anna Szabó (Ph.D. Student), and Dr. Klára Magyari for their help during the recording of the XRD patterns. The authors also wish to thank Dr. Mariann Kis for recording the flash kinetics measurements, respectively Dr. Kata Hajdu and Richárd Csekő (MSc Student), to help during the preparation of biocomposites. Biborka Boga thanks the financial support provided by Babeș-Bolyai University *via* the scholarship 'Bursă Specială pentru Activitatea Științifică' during the 2019-2020 academic year. István Székely wishes to express his gratitude to the Romanian National Authority for Scientific Research, CNCS–UEFISCDI, project number PN-III-P1-1.1-MC-2018-3361, respectively to the Hungarian Academy of Sciences "Domus Junior" scholarship. The European Union and the State of Hungary supported a part of the research, co-financed by the

European Regional Development Fund in GINOP-2.3.2.-15-2016-00009 'ICER'.

Authors' contribution

Bíborka Boga: Writing – original draft, review & editing, Formal analysis, Investigation. **István Székely**: Investigation, Writing – review & editing. **Monica Focșan**: Investigation, Writing – review & editing. **Monica Baia**: Writing – review & editing. **Tibor Szabó**: Investigation, Funding acquisition. **László Nagy**: Investigation, Writing – review & editing, Funding acquisition. **Zsolt Pap**: Conceptualization, Writing – review & editing, Funding acquisition.

Data availability

The corresponding author will provide the experimental data in the case of a reasonable request.

Declaration of competing interest

No competing financial interests exists between the authors

References

[1] L. Ricotti, A. Menciassi, K. Morishima, Guest editorial introduction to the Special Issue on bio-hybrid systems and living machines, Biomed. Microdevices. 14 (2012) 965–967. https://doi.org/10.1007/s10544-012-9722-z.

[2] S.-R. E., Interdisciplinarity: Bring biologists into biomimetics., Nature. 529 (2016) 277–8.

[3] K. Hajdu, T. Szabó, A.E. Sarrai, L. Rinyu, L. Nagy, Functional Nanohybrid Materials from Photosynthetic Reaction Center Proteins, Int. J. Photoenergy. 2017 (2017) 9128291. https://doi.org/10.1155/2017/9128291.

[4] R.E. Blankenship, Early evolution of photosynthesis, Plant Physiol. 154 (2010) 434–438. https://doi.org/10.1104/pp.110.161687.

[5] L. Nagy, K. Hajdu, B. Fiser, K. Hernadi, Photosynthetic Reaction Centres-from Basic Research to Application, Not. Sci. Biol. 2 (2010) 07–13. https://doi.org/10.15835/nsb224660.

[6] K. Hajdu, C. Gergely, M. Martin, T. Cloitre, L. Zimányi, K. Tenger, P. Khoroshyy, G. Palestino, V. Agarwal, K. Hernádi, Z. Németh, L. Nagy, Porous silicon/photosynthetic reaction center hybrid nanostructure, Langmuir. 28 (2012) 11866–11873. https://doi.org/10.1021/la301888p.

[7] Y. Lu, M. Yuan, Y. Liu, B. Tu, C. Xu, B. Liu, D. Zhao, J. Kong, Photoelectric Performance of Bacteria Photosynthetic Proteins Entrapped on Tailored Mesoporous WO_3-TiO_2 Films, Langmuir. 21 (2005) 4071–4076. https://doi.org/10.1021/la0470129.

[8] T. Szabó, G. Bencsik, M. Magyar, C. Visy, Z. Gingl, K. Nagy, G. Váró, K. Hajdu, G. Kozák, L. Nagy, Photosynthetic reaction centers/ITO hybrid nanostructure, Mater. Sci. Eng. C. 33 (2013) 769–773. https://doi.org/https://doi.org/10.1016/j.msec.2012.10.031.

[9] T. Szabó, M. Magyar, Z. Németh, K. Hernádi, B. Endrődi, G. Bencsik, C. Visy, E. Horváth, A. Magrez, L. Forró, L. Nagy, Charge stabilization by reaction center protein immobilized to carbon nanotubes functionalized by amine groups and poly(3-thiophene acetic acid) conducting polymer, Phys. Status Solidi. 249 (2012) 2386–2389. https://doi.org/10.1002/pssb.201200118.

[10] Y. Kim, S.A. Shin, J. Lee, K.D. Yang, K.T. Nam, Hybrid system of semiconductor and photosynthetic protein, Nanotechnology. 25 (2014) 342001. https://doi.org/10.1088/0957-4484/25/34/342001.

[11] M. Dorogi, Z. Bálint, C. Mikó, B. Vileno, M. Milas, K. Hernádi, L. Forró, G. Váró, L. Nagy, Stabilization Effect of Single-Walled Carbon Nanotubes on the Functioning of Photosynthetic Reaction Centers, J. Phys. Chem. B. 110 (2006) 21473–21479. https://doi.org/10.1021/jp060828t.

[12] L. Nagy, M. Magyar, T. Szabó, K. Hajdu, L. Giotta, M. Dorogi, F. Milano, Photosynthetic machineries in nano-systems, Curr. Protein Pept. Sci. 15 (2014) 363–373. https://doi.org/10.2174/1389203715666140327102757.

[13] H.A. Heering, F.G.M. Wiertz, C. Dekker, S. de Vries, Direct Immobilization of Native Yeast Iso-1 Cytochrome c on Bare Gold: Fast Electron Relay to Redox Enzymes and Zeptomole Protein-Film Voltammetry, J. Am. Chem. Soc. 126 (2004) 11103–11112. https://doi.org/10.1021/ja046737w.

[14] R.C. Prince, R.J. Cogdell, A.R. Crofts, The photo-oxidation of horse heart cytochrome c and native cytochrome c2 by reaction centres from Rhodopseudomonas spheroides R26, Biochim. Biophys. Acta - Bioenerg. 347 (1974) 1–13. https://doi.org/https://doi.org/10.1016/0005-2728(74)90194-7.

[15] S. Shi, Z. Sun, C. Bao, T. Gao, Y.H. Hu, The special route toward conversion of methane to methanol on a fluffy metal-free carbon nitride photocatalyst in the presence of H_2O_2, Int. J. Energy Res. 44 (2020) 2740–2753. https://doi.org/10.1002/er.5088.

[16] T.L. Olson, J.C. Williams, J.P. Allen, Influence of protein interactions on oxidation/reduction midpoint potentials of cofactors in natural and de novo metalloproteins, Biochim. Biophys. Acta - Bioenerg. 1827 (2013) 914–922. https://doi.org/10.1016/j.bbabio.2013.02.014.

[17] J.C. Durán-Álvarez, R. Zanella, S. OROS-RUÍZ, Heterogeneous Gold Catalysts and Catalysis, Royal Society of Chemistry, 2014. https://doi.org/10.1039/9781782621645.

[18] B. Boga, I. Székely, Z. Pap, L. Baia, M. Baia, Detailed Spectroscopic and Structural Analysis of TiO_2/WO_3 Composite Semiconductors, J. Spectrosc. 2018 (2018). https://doi.org/10.1155/2018/6260458.

[19] L. Baia, E. Orbán, S. Fodor, B. Hampel, E.Z. Kedves, K. Saszet, I. Székely, É. Karácsonyi, B. Réti, P. Berki, A. Vulpoi, K. Magyari, A. Csavdári, C. Bolla, V. Coșoveanu, K. Hernádi, M. Baia, A. Dombi, V. Danciu, G. Kovács, Z. Pap, Preparation of TiO_2/WO_3 composite photocatalysts by the adjustment of the semiconductors' surface charge, Mater. Sci.

Semicond. Process. 42 (2016) 66–71. https://doi.org/https://doi.org/10.1016/j.mssp.2015.08.042.

[20] I. Székely, G. Kovács, L. Baia, V. Danciu, Z. Pap, Synthesis of Shape-Tailored WO_3 Micro-/Nanocrystals and the Photocatalytic Activity of WO_3/TiO_2 Composites, Materials (Basel). 9 (2016) 258. https://doi.org/10.3390/ma9040258.

[21] E.-Z. Kedves, I. Székely, L. Baia, M. Baia, A. Csavdári, Z. Pap, The Comparison of the Photocatalytic Performance Shown by TiO_2 and TiO_2/WO_3 Composites — A Parametric and Kinetic Study, J. Nanosci. Nanotechnol. 19 (2018) 356–365. https://doi.org/10.1166/jnn.2019.15792.

[22] W.H. Lee, C.W. Lai, S.B.A. Hamid, One-Step Formation of WO_3-Loaded TiO_2 Nanotubes Composite Film for High Photocatalytic Performance, Materials (Basel). 8 (2015) 2139–2153. https://doi.org/10.3390/ma8052139.

[23] J. Luo, M. Hepel, Photoelectrochemical degradation of naphthol blue black diazo dye on WO_3 film electrode, Electrochim. Acta. 46 (2001) 2913–2922. https://doi.org/https://doi.org/10.1016/S0013-4686(01)00503-5.

[24] A.A. Rashid, N.H. Saad, D. Bien, C. Sheng, M. Azad, M. Akhir, Hydrothermal Synthesis Of Tungsten Oxide (WO 3) Nanostructures Using Sodium Chloride As Structure Directing Agent, 2015. www.jmest.org (accessed March 9, 2021).

[25] X.C. Song, Y.F. Zheng, E. Yang, Y. Wang, Large-scale hydrothermal synthesis of WO_3 nanowires in the presence of K_2SO_4, Mater. Lett. 61 (2007) 3904–3908. https://doi.org/10.1016/j.matlet.2006.12.055.

[26] X. Gao, C. Yang, F. Xiao, Y. Zhu, J. Wang, X. Su, $WO_3 \cdot 0.33H_2O$ nanoplates: Hydrothermal synthesis, photocatalytic and gas-sensing properties, Mater. Lett. 84 (2012) 151–153. https://doi.org/https://doi.org/10.1016/j.matlet.2012.06.078.

[27] I. Székely, M. Baia, K. Magyari, B. Boga, Z. Pap, The effect of the pH adjustment upon the WO_3-$WO_3 \cdot 0.33H_2O$-TiO_2 ternary composite systems' photocatalytic activity, Appl. Surf. Sci. 490 (2019) 469–480. https://doi.org/https://doi.org/10.1016/j.apsusc.2019.06.036.

[28] P. Maróti, C.A. Wraight, Flash-induced H+ binding by bacterial photosynthetic reaction centers: Influences of the redox states of the acceptor quinones and primary donor, Biochim. Biophys. Acta - Bioenerg. 934 (1988) 329–347. https://doi.org/https://doi.org/10.1016/0005-2728(88)90092-8.

[29] A.L. Patterson, The Scherrer Formula for X-Ray Particle Size Determination, Phys. Rev. 56 (1939) 978–982. https://doi.org/10.1103/PhysRev.56.978.

[30] J. Tandori, L. Nagy, Á. Puskás, M. Droppa, G. Horváth, P. Maróti, The IleL229 → Met mutation impairs the quinone binding to the QB-pocket in reaction centers of Rhodobacter sphaeroides, Photosynth. Res. 45 (1995) 135–146. https://doi.org/10.1007/BF00032585.

[31] T. Szabo, R. Panajotović, J. Vujin, T. Tomašević-Ilić, I. Bagdanavičitūtė, G. Urbonaitė, R. Cseko, K. Hernadi, G. Varo, L. Nagy, Photosynthetic Reaction-Center/Graphene Biohybrid for Optoelectronics, J. Nanosci. Nanotechnol. 21 (2021) 2342–2350. https://doi.org/10.1166/JNN.2021.18976.

[32] S.K. Biswas, J.-O. Baeg, A facile one-step synthesis of single crystalline hierarchical WO3 with enhanced activity for photoelectrochemical solar water oxidation, Int. J. Hydrogen Energy. 38 (2013) 3177–3188. https://doi.org/https://doi.org/10.1016/j.ijhydene.2012.12.114.

[33] J. Wang, E. Khoo, P.S. Lee, J. Ma, Controlled Synthesis of WO3 Nanorods and Their Electrochromic Properties in H_2SO_4 Electrolyte, J. Phys. Chem. C. 113 (2009) 9655–9658. https://doi.org/10.1021/jp901650v.

[34] Q. Xiang, G.F. Meng, H.B. Zhao, Y. Zhang, H. Li, W.J. Ma, J.Q. Xu, Au Nanoparticle Modified WO3 Nanorods with Their Enhanced Properties for Photocatalysis and Gas Sensing, J. Phys. Chem. C. 114 (2010) 2049–2055. https://doi.org/10.1021/jp909742d.

[35] K.J. Lethy, D. Beena, R. Vinod Kumar, V.P. Mahadevan Pillai, V. Ganesan, V. Sathe, Structural, optical and morphological studies on laser ablated nanostructured WO_3 thin films, Appl. Surf. Sci. 254 (2008) 2369–2376. https://doi.org/10.1016/j.apsusc.2007.09.068.

[36] S. Salmaoui, F. Sediri, N. Gharbi, Characterization of h-WO_3 nanorods synthesized by hydrothermal process, Polyhedron. 29 (2010) 1771–1775. https://doi.org/https://doi.org/10.1016/j.poly.2010.02.025.

[37] M.F. Daniel, B. Desbat, J.C. Lassegues, B. Gerand, M. Figlarz, Infrared and Raman study of WO3 tungsten trioxides and WO3, xH2O tungsten trioxide tydrates, J. Solid State Chem. 67 (1987) 235–247. https://doi.org/https://doi.org/10.1016/0022-4596(87)90359-8.

[38] A. Rougier, F. Portemer, A. Quédé, M. El Marssi, Characterization of pulsed laser deposited WO3 thin films for electrochromic devices, Appl. Surf. Sci. 153 (1999) 1–9.

https://doi.org/https://doi.org/10.1016/S0169-4332(99)00335-9.

[39] E. Valova, J. Georgieva, S. Armyanov, S. Sotiropoulos, A. Hubin, K. Baert, M. Raes, Morphology, Structure and Photoelectrocatalytic Activity of TiO_2/WO_3 Coatings Obtained by Pulsed Electrodeposition onto Stainless Steel, J. Electrochem. Soc. 157 (2010) D309. https://doi.org/10.1149/1.3356001.

[40] K. Kalantar-Zadeh, A. Vijayaraghavan, M.H. Ham, H. Zheng, M. Breedon, M.S. Strano, Synthesis of atomically thin WO_3 sheets from hydrated tungsten trioxide, Chem. Mater. 22 (2010) 5660–5666. https://doi.org/10.1021/cm1019603.

[41] C.G. Granqvist, Handbook of Inorganic Electrochromic Materials, Elsevier, 1995.

[42] B. Pecquenard, H. Lecacheux, J. Livage, C. Julien, Orthorhombic WO_3 Formed via a Ti-Stabilized $WO_3 \cdot 13H_2O$ Phase, J. Solid State Chem. 135 (1998) 159–168. https://doi.org/https://doi.org/10.1006/jssc.1997.7618.

[43] W. Weltner, D. McLeod, Spectroscopy of tungsten oxide molecules in neon and argon matrices at 4° and 20°K, J. Mol. Spectrosc. 17 (1965) 276–299. https://doi.org/10.1016/0022-2852(65)90167-0.

[44] E. Salje, Lattice dynamics of WO3, Acta Crystallogr. Sect. A. 31 (1975) 360–363. https://doi.org/10.1107/S0567739475000757.

[45] K. Ohwada, Lattice vibrations of δ-uranium and tungsten trioxides, Spectrochim. Acta Part A Mol. Spectrosc. 26 (1970) 1035–1044. https://doi.org/https://doi.org/10.1016/0584-8539(70)80005-8.

[46] S. Bai, K. Zhang, L. Wang, J. Sun, R. Luo, D. Li, A. Chen, Synthesis mechanism and gas-sensing application of nanosheet-assembled tungsten oxide microspheres, J. Mater. Chem. A. 2 (2014) 7927–7934. https://doi.org/10.1039/C4TA00053F.

[47] S. Badilescu, Infrared ATR Spectroscopic Studies on Hydrated Tungsten Oxide Thin Films, J. Electrochem. Soc. 136 (1989) 3599. https://doi.org/10.1149/1.2096516.

[48] K. Gibasiewicz, R. Naskręcki, M. Ziółek, M. Lorenc, J. Karolczak, J. Kubicki, J. Goc, J. Miyake, A. Dobek, Electron Transfer in the Reaction Center of the Photosynthetic Bacterium Rb. sphaeroides R-26 Measured by Transient Absorption in the Blue Spectral Range, J. Fluoresc. 11 (2001) 33–40. https://doi.org/10.1023/A:1016695515341.

[49] Y. Negishi, S. Watanabe, M. Aoki, S. Hossain, W. Kurashige, Toward the Creation of Highly Active Photocatalysts That Convert Methane into Methanol, in: M. Rahman, A.

Khan, A. Asiri, I. Inamuddin (Eds.), Concepts Semicond. Photocatal., IntechOpen, Rijeka, 2019. https://doi.org/10.5772/intechopen.85335.

[50] T.L. Olson, J.C. Williams, J.P. Allen, Influence of protein interactions on oxidation/reduction midpoint potentials of cofactors in natural and de novo metalloproteins, Biochim. Biophys. Acta - Bioenerg. 1827 (2013) 914–922. https://doi.org/https://doi.org/10.1016/j.bbabio.2013.02.014.

[51] B.A.-L. Liu Baixiong A4 - Wang, Jinshu A4 - Wu, Junshu A4 - Li, Hongyi A4 - Li, Zhifei A4 - Zhou, Meiling A4 - Zuo, Tieyong, Controlled fabrication of hierarchical WO_3 hydrates with excellent adsorption performance, J. Mater. Chem. A. v. 2 (2014) 1947-1954–2014 v.2 no.6. https://doi.org/10.1039/c3ta13897f.

[52] S. Prabhu, A. Nithya, S.C. Mohan, K. Jothivenkatachalam, Synthesis, Surface Acidity and Photocatalytic Activity of WO_3/TiO_2 Nanocomposites – An Overview, Mater. Sci. Forum. 781 (2014) 63–78. https://doi.org/10.4028/www.scientific.net/MSF.781.63.

[53] K. Hajdu, T. Szabó, M. Magyar, G. Bencsik, Z. Németh, K. Nagy, A. Magrez, L. Forró, G. Váró, K. Hernádi, L. Nagy, Photosynthetic reaction center protein in nanostructures, Phys. Status Solidi. 248 (2011) 2700–2703. https://doi.org/10.1002/pssb.201100046.

[54] V.P. Shinkarev, C.A. Wraight, The interaction of quinone and detergent with reaction centers of purple bacteria. I. Slow quinone exchange between reaction center micelles and pure detergent micelles, Biophys. J. 72 (1997) 2304–2319. https://doi.org/10.1016/S0006-3495(97)78875-1.

[55] A. Agostiano, F. Milano, M. Trotta, Investigation on the detergent role in the function of secondary quinone in bacterial reaction centers, Eur. J. Biochem. 262 (1999) 358–364. https://doi.org/10.1046/j.1432-1327.1999.00366.x.

[56] W.L. Courchene, Micellar Properties from Hydrodynamic Data, J. Phys. Chem. 68 (1964) 1870–1874. https://doi.org/10.1021/j100789a034.

[57] C.A. Wraight, R.J. Shopes, Quinone Binding and Herbicide Activity in the Acceptor Quinone Complex of Bacterial Reaction Centres, in: Tech. New Dev. Photosynth. Res., Springer US, 1989: pp. 183–191. https://doi.org/10.1007/978-1-4684-8571-4_22.

[58] L. Nagy, F. Milano, M. Dorogi, A. Agostiano, G. Laczkó, K. Szebényi, G. Váró, M. Trotta, P. Maróti, Protein/lipid interaction in the bacterial photosynthetic reaction center: Phosphatidylcholine and phosphatidylglycerol modify the free energy levels of the

quinones, Biochemistry. 43 (2004) 12913–12923. https://doi.org/10.1021/bi0489356.

[59] P.V.K. Yadav, Y.A.K. Reddy, B. Ajitha, V.R. Minnam Reddy, Oxygen partial pressure dependent UV photodetector performance of WO_3 sputtered thin films, J. Alloys Compd. 816 (2020) 152565. https://doi.org/10.1016/J.JALLCOM.2019.152565.

[60] I. Székely, E.-Z. Kedves, Z. Pap, M. Baia, Synthesis Design of Electronegativity Dependent WO_3 and $WO_3 \cdot 0.33H_2O$ Materials for a Better Understanding of TiO_2/WO_3 Composites' Photocatalytic Activity, Catal. 2021, Vol. 11, Page 779. 11 (2021) 779. https://doi.org/10.3390/CATAL11070779.

[61] Y.A.K. Reddy, B. Ajitha, A. Sreedhar, E. Varrla, Enhanced UV photodetector performance in bi-layer TiO_2/WO_3 sputtered films, Appl. Surf. Sci. 494 (2019) 575–582. https://doi.org/10.1016/J.APSUSC.2019.07.124.

[62] P.V.K. Yadav, B. Ajitha, Y.A.K. Reddy, V.R.M. Reddy, Enhanced Performance of WO_3 Photodetectors Through Hybrid Graphene-Layer Integration, ACS Appl. Electron. Mater. (2021). https://doi.org/10.1021/ACSAELM.1C00073.

[63] Y.A.K. Reddy, B. Ajitha, M. Reddeppa, A. Sreedhar, Improvement of UV photodetector properties of reactively sputtered TiO_{2-x} films through vacuum annealing, J. Mater. Sci. Mater. Electron. 2019 3023. 30 (2019) 20687–20695. https://doi.org/10.1007/S10854-019-02434-2.

[64] P. V. Karthik Yadav, B. Ajitha, Y.A.K. Reddy, V.R. Minnam Reddy, M. Reddeppa, M.D. Kim, Effect of sputter pressure on UV photodetector performance of WO_3 thin films, Appl. Surf. Sci. 536 (2021) 147947. https://doi.org/10.1016/J.APSUSC.2020.147947.

[65] R.I. Gelb, Conductometric determination of pKa values. Oxalic and squaric acids, Anal. Chem. 43 (2002) 1110–1113. https://doi.org/10.1021/AC60303A028.

[66] Y. AlSalka, A. Hakki, M. Fleisch, D.W. Bahnemann, Understanding the degradation pathways of oxalic acid in different photocatalytic systems: Towards simultaneous photocatalytic hydrogen evolution, J. Photochem. Photobiol. A Chem. 366 (2018) 81–90. https://doi.org/10.1016/J.JPHOTOCHEM.2018.04.008.

[67] P. V. Karnat, Electrochromic and Photoelectrochromic Aspects of Semiconductor Nanostructure-Molecular Assembly, in: Electrochem. Nanomater., Wiley-VCH Verlag GmbH, Weinheim, Germany, 2007: pp. 229–246. https://doi.org/10.1002/9783527612789.ch08.

[68] K. Dai, H. Chen, T. Peng, D. Ke, H. Yi, Photocatalytic degradation of methyl orange in aqueous suspension of mesoporous titania nanoparticles, Chemosphere. 69 (2007) 1361–1367. https://doi.org/https://doi.org/10.1016/j.chemosphere.2007.05.021.

[69] R. Shan, L. Lu, J. Gu, Y. Zhang, H. Yuan, Y. Chen, B. Luo, Photocatalytic degradation of methyl orange by Ag/TiO2/biochar composite catalysts in aqueous solutions, Mater. Sci. Semicond. Process. 114 (2020) 105088. https://doi.org/10.1016/J.MSSP.2020.105088.

[70] C. Nie, J. Dong, P. Sun, C. Yan, H. Wu, B. Wang, An efficient strategy for full mineralization of an azo dye in wastewater: a synergistic combination of solar thermo- and electrochemistry plus photocatalysis, RSC Adv. 7 (2017) 36246–36255. https://doi.org/10.1039/C7RA05797K.

Appendices

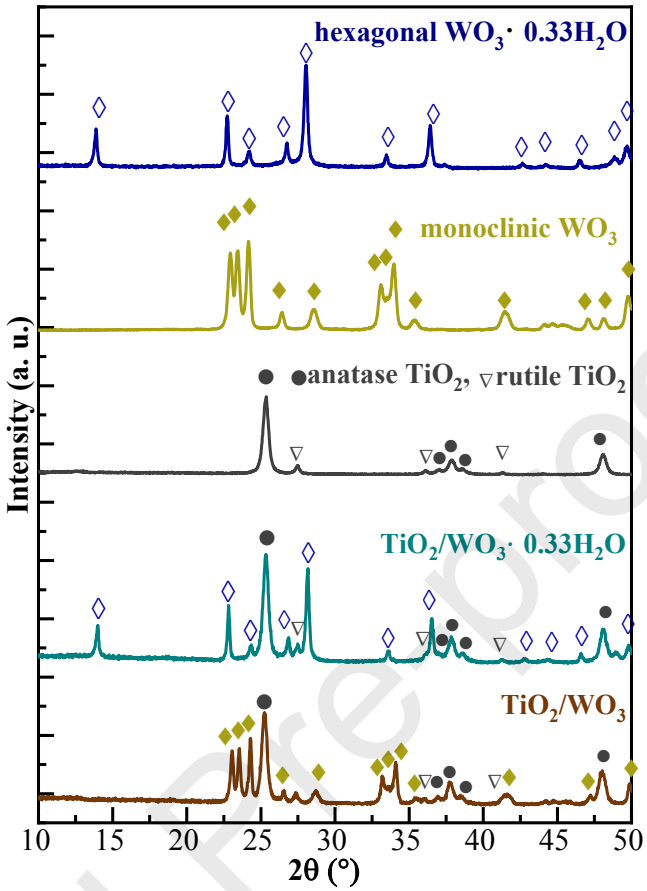

Fig. A1. The XRD pattern of $WO_3 \cdot 0.33H_2O$, WO_3 and TiO_2, respectively $TiO_2/WO_3 \cdot 0.33H_2O$ and TiO_2/WO_3 composites

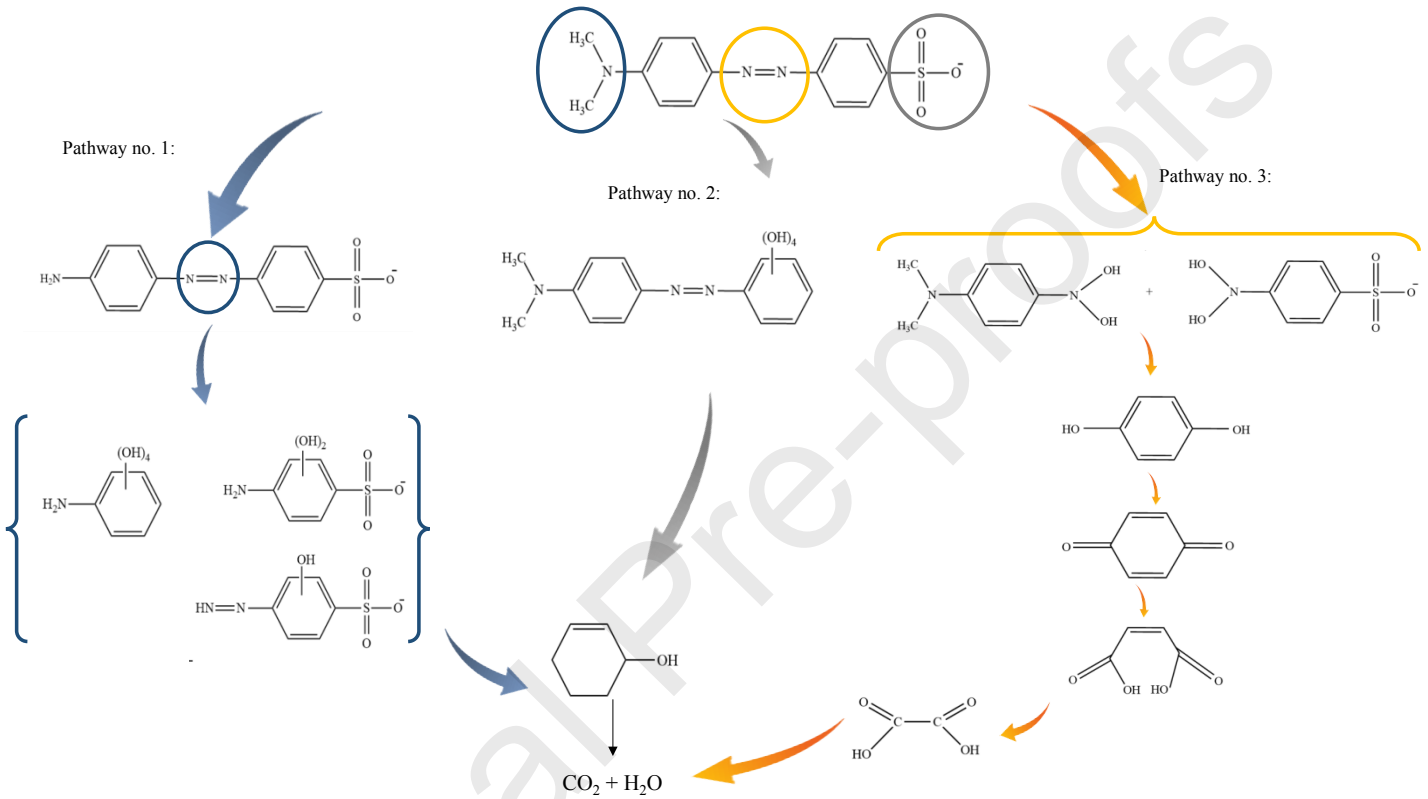

Fig. A2. The proposed pathways for MO degradation (Pathway no. 1 and 2 [66], Pathway no. 3[70])